

Observation of charge to spin conversion in p-orbital InBi alloy

Gen Li^{1†}, Ying Zhang^{2,3†}, Xiaoguang Xu^{1*}, Lei Shen^{4,3*}, Zheng Feng⁵, Kangkang Meng¹, Ang Li⁶, Lu Cheng¹, Kang He⁵, Wei Tan⁵, Yong Wu¹, Yihong Wu^{2,3}, Yong Jiang^{1,7*}

¹Key Laboratory of Advanced Materials and Devices for Post-Moore Chips, Ministry of Education, School of Materials Science and Engineering, University of Science and Technology Beijing; Beijing 100083, China.

²Department of Electrical and Computer Engineering, National University of Singapore; 117576 Singapore.

³National University of Singapore (Chong Qing) Research Institute; Chongqing Liang Jiang New Area, Chongqing 401123, China.

⁴Department of Mechanical Engineering, National University of Singapore; 117575 Singapore.

⁵Microsystem & Terahertz Research Center, CAEP; Chengdu 610200, China.

⁶Faculty of Materials and Manufacturing, Beijing Key Lab of Microstructure and Properties of Advanced Materials, Beijing University of Technology; Beijing 100124, China.

⁷Institute of Quantum Materials and Devices, School of Electronic and Information Engineering; State Key Laboratory of Separation Membranes and Membrane Processes, Tiangong University; Tianjin 300387, China.

*Corresponding author. Email: xgxu@ustb.edu.cn (X.G.X.); shenlei@nus.edu.sg (L.S.); yjiang@ustb.edu.cn (Y.J.)

[†]These authors contributed equally to this work.

High density data storage and spin-logic devices require highly efficient all-electric control of spin moment. So far, charge-to-spin conversion through the spin Hall effect limits to d-orbital materials associated with strong spin-orbit coupling, especially heavy metals. However, d-orbital heavy metals with strong spin-orbit coupling results in a short spin diffusion length, which restricts the spin transport and accumulation in spintronic devices. Therefore, the conflict between charge-to-spin conversion efficiency and spin transport ability is irreconcilable in d-orbital materials. Here, we report a large charge to spin conversion experimentally observed in the p-orbital In_2Bi alloy, exhibiting the coexistence of a large spin Hall angle comparable to heavy metal Pt and a long spin diffusion length (4 times that of Pt). First-principles calculations reveal that topological symmetry-protected gap opening near the Fermi level results in large Berry curvature-related spin Hall conductivity. Due to the delocalized nature of p-orbitals and semimetal properties of In_2Bi , its spin current can overcome the physical barriers between spin Hall angle and spin diffusion length in d-orbital metals, thereby advancing the development of high-performance spintronic devices.

Highly efficient charge-to-spin conversion is a major scientific issue for future spintronic devices. The spin Hall effect (SHE) is a well-known source of spin current by separating spin electrons to opposite material surfaces. Conventionally, d-orbital heavy metals (HM) enable the SHE due to their strong spin-orbit coupling (SOC)¹⁻³. Upon injection into adjacent ferromagnetic (FM) layers, these spin currents induce spin-orbit torque (SOT) to switch the magnetization of the FM layer⁴⁻⁸. Therefore, the spin current generation and its transportation within HM/FM interface dominant the performance of the SOT-based spintronic devices⁹⁻¹².

Traditionally, heavy 5d transition metals with strong SOC and large spin Hall angle (SHA, θ_{SH}), such as Ta^{13, 14}, W¹⁵⁻¹⁸ and Pt¹⁹⁻²², are primary spin current sources. However, the localized d-orbital and strong SOC scattering to electrons result in short spin diffusion length (SDL, λ) in these heavy metals. This significantly restricts the effective propagation of spin currents, as illustrated in Fig. 1a, and their spintronic applications.

The intrinsic Berry curvature plays a key role in spin current generation via SHE²³⁻²⁶, which induces non-uniform electron motion in the energy bands, resulting in transverse spin accumulation. The bismuth and its compounds have been reported to be topological semimetals with large Berry curvature²⁷⁻³⁰ or spin Nernst effect³¹. Meanwhile, only containing p-orbital elements facilitates the propagation of spin current and result in a large λ .

In this study, a p-orbital In₂Bi alloy is proved to be a spin current source material via SHE both theoretically and experimentally (Fig. 1b). Our spin transport experiments

show that the SHA of In₂Bi is comparable to that of Pt, while its SDL is 4 times as much as that of Pt. First-principles calculations reveal that In₂Bi has unique topological band structures, delocalized p-bands near the Fermi level, and a large Berry curvature, which accounts for the coexistence of large SHA and long SDL. The observation of p-orbital spin current in In₂Bi overcomes the physical limitation of spin current sources in heavy 5d transition metals and expands the possibilities for designing new SOT-based spintronic devices.

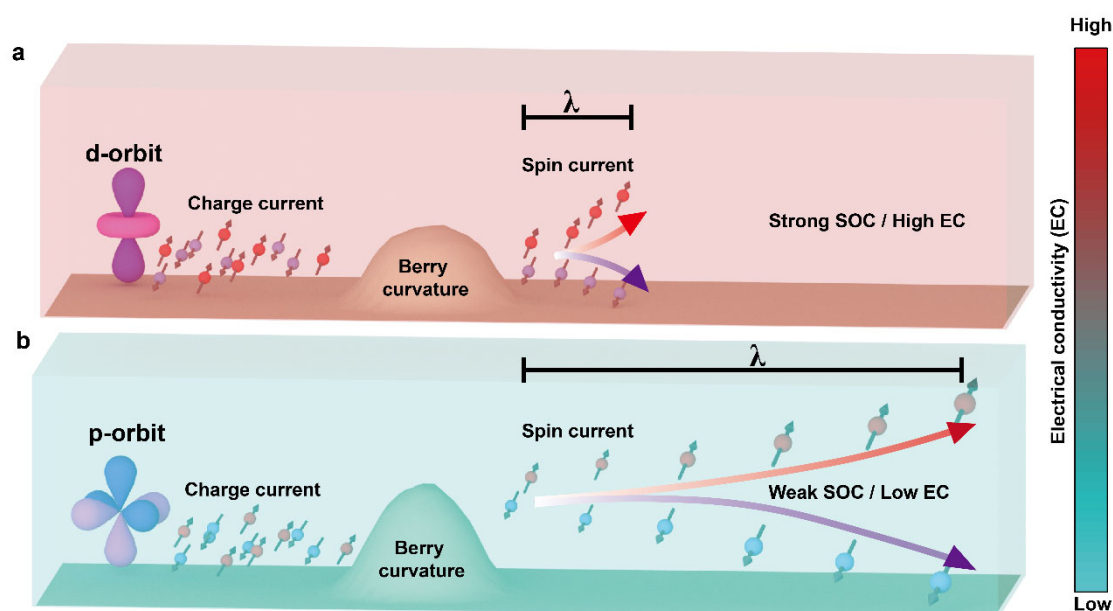


Fig. 1. Physical mechanisms of d-orbital and p-orbital materials. **a**, Traditional d-orbital spin current source materials and **b**, p-orbital spin current source materials. The color bar represents the electrical conductivity (EC) levels of materials.

In₂Bi synthesis and characterization

In₂Bi films with thicknesses ranging from 3 to 40 nm were deposited on Si/SiO₂

substrates by using magnetron sputtering. The roughness of the In₂Bi film is tested by atomic force microscopy (AFM). The 2D and 3D images of a 13 nm In₂Bi and 3 nm Co films shown in Fig. S1 reveals that In₂Bi grows into a granular film with a root mean square roughness R_q of approximately 2.50 nm, and Co with a roughness R_q of 0.28 nm. Moreover, the In₂Bi film is test to be insulated, supporting the granular character of the In₂Bi film. Grazing incidence X-ray diffraction (GI-XRD) pattern presented in Fig. 2a is well consistent with the standard PDF card of In₂Bi (PDF: 71-227), revealing good crystallinity of the film. Meanwhile, the enhanced diffraction intensity of (102) peak indicates a preferred orientation of the film. Considering the potential sensitivity of measurements to interface roughness, In₂Bi is deposited on the Co layer to achieve a uniform and smooth In₂Bi /Co interface for the spin transport measurements.

X-ray photoelectron spectroscopy (XPS) measurements are conducted to decide the binding state of the In₂Bi and the XPS spectra for In and Bi elements were calibrated against carbon. Fig. 2b shows the XPS spectrum of the outer-shell orbitals of In and Bi near the Fermi level, together with the fitting curves. The peaks observed within the binding energy range of -5 eV to 35 eV correspond to 5p and 4d orbitals of In, as well as the 6p, 6s, and 5d orbitals of Bi. Fig. 2c provides a magnified view of the binding energy region from -5 eV to 12.5 eV, highlighting that the 5p orbital of In and the 6p orbital of Bi locate close to the Fermi level. Comparing to d-orbital, p-orbital of In and Bi take on an obviously delocalized character. The In 3d and Bi 4f core level spectra (Fig. 2d and 2e) indicate that the film is composed by In and Bi elements only.

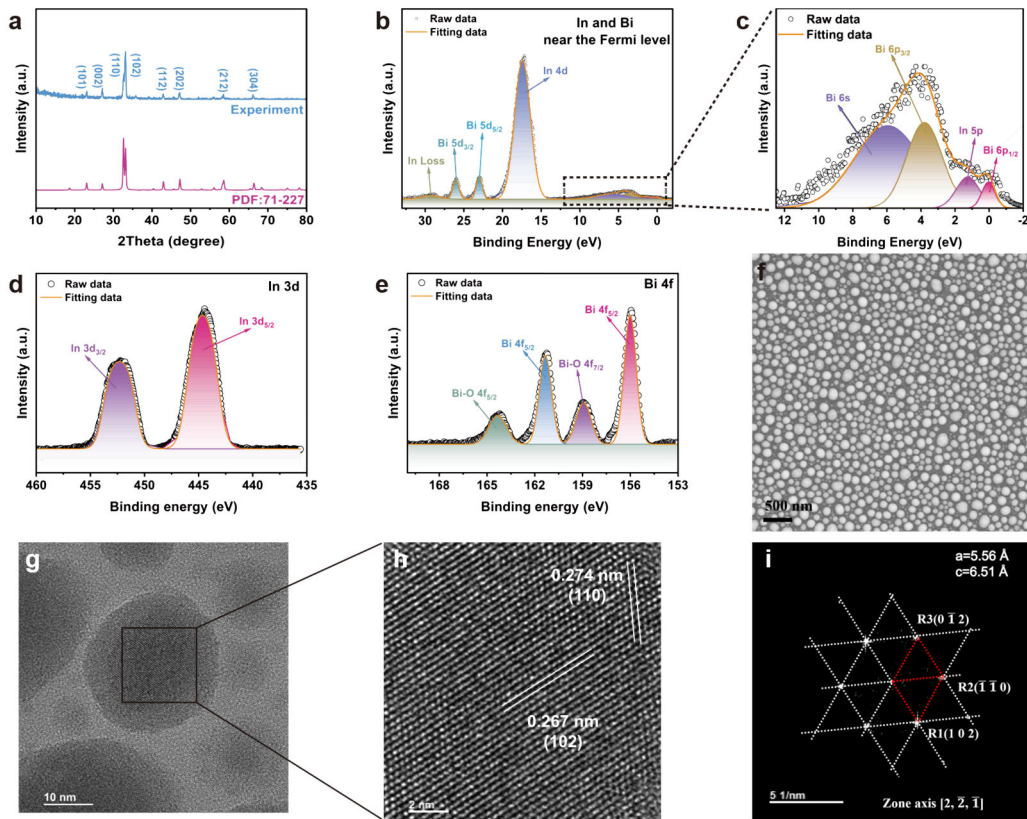


Fig. 2. Composition and crystallization structure of In_2Bi thin films. **a**, XRD pattern of In_2Bi film grown on Si/SiO_2 substrate, together with PDF card (number: 71-227). **b**, XPS spectrum for Bi and In near the Fermi level in In_2Bi . **c**, XPS spectrum of the binding energy range from -5 eV to 12.5 eV. **d**, In 3d and **e**, Bi 4f XPS spectra of In_2Bi . **f**, SEM image of 13 nm In_2Bi film. **g**, TEM image of 13 nm In_2Bi single particle, **h**, enlarged TEM image and **i**, selected area diffraction pattern of the corresponding area.

The scanning electron microscope (SEM) image in Fig. 2f clearly shows that the In_2Bi film grown on the Si/SiO_2 substrate exhibits a granular morphology, consistent with the result of AFM. Transmission electron microscopy (TEM) characterization was performed on In_2Bi film and the images are presented in Fig. 2g and Fig. 2h. The

granular film is composed by single crystals, with the size ranging mainly from 30 to 40 nm. Fig. 2h shows good lattice structure of a single particle which can be indexed to (102) and (110). The diffraction pattern in Fig. 2i can be indexed into (102), ($\bar{1}\bar{1}0$), and ($0\bar{1}2$), indicating a hexagonal crystal structure of In₂Bi. According to the TEM and XRD results, the In₂Bi particles prefer to grow along (102) plane during sputtering. Energy dispersive spectroscopy (EDS) mapping analysis in Fig. S2 further demonstrates the content of In and Bi in the film. Moreover, the stoichiometry of the film is defined to be In₂Bi by semi-quantitative element content comparison based on the In₂Bi XPS spectra and quantitatively inductively coupled plasma optical emission spectrometer (ICP-OES) (See Supplementary Note 1 and Fig. S3).

Spin Hall angle and spin diffusion length measurements

spin Hall magnetoresistance (SMR) measurements are employed to examine the spin current generation and diffusion in In₂Bi, as shown in Fig. 3a. The influence of the Co/ In₂Bi interface alloying on the SMR is excluded by sweeping field tests as shown in Fig. S4. The specific mechanism of SMR testing is shown in Supplementary Note 2. Specifically, Hall bar devices were fabricated on a Si/SiO₂ substrate with the stacking structure of Co (3)/ In₂Bi (t)/Al₂O₃ (thickness in nanometer, t=0, 3, 5, 7, 9, 11, 13, 15, 17, 25, and 40). The SMR curve for each In₂Bi thickness is shown in Supplementary Note 3 and Fig. S5, together with fitting curves. As summarized in Fig. 3b and Fig. 3c, the SMR signal increases gradually with the thickness of In₂Bi and reaches the maximum of approximately 0.093% when t = 13 nm. Subsequently, the signal decreases

with the thickness further increasing. The relationship between the thickness and the extracted SMR signal for the FM/NM heterojunction can be expressed as follows:

$$\frac{\Delta R_{XX}^{SMR}}{R_{XX}^0} \sim -\theta_{SH}^2 \frac{\lambda_N}{t_N} \frac{\tanh^2\left(\frac{t_N}{2\lambda_N}\right)}{1+\xi} \times \left[\frac{g_R}{1+g_R \coth\left(\frac{t_N}{\lambda_N}\right)} - \frac{g_F}{1+g_F \coth\left(\frac{t_N}{\lambda_N}\right)} \right] \quad (1)$$

$$g_R \equiv 2\rho_N \lambda_N \text{Re}[G_{MIX}] , \quad g_F \equiv \frac{(1-P^2)\rho_N \lambda_N}{\rho_F \lambda_F \coth\left(\frac{t_F}{\lambda_F}\right)}$$

Here, R^0 denotes the resistance when the magnetization is aligned along the Z-axis. The variables t_N 、 ρ_N 、 λ_N , and θ_{SH} represent the thickness, resistivity, spin diffusion length, and spin Hall angle of the non-magnetic layer, respectively. G_{MIX} refers to the spin mixing conductance. Additionally, t_F 、 ρ_F 、 λ_F , and P correspond to the thickness, resistivity, SDL, and spin polarization of the ferromagnetic layer, respectively. The parameter ξ describes the shunting effect entering the magnetic layer and can be expressed as $\frac{\rho_{NM}d_{FM}}{\rho_{FM}d_{NM}}$.

We employed Equation (1) to analyze the variation trend of SMR in the Co (3)/In₂Bi (t)/Al₂O₃ heterojunction. The fitting results are well consistent with experimental data for different In₂Bi thickness. Meanwhile, the θ_{SH} and λ of In₂Bi are defined to be 0.07 and 4.64 nm, respectively. According to the SMR results, the θ_{SH} of In₂Bi alloy is comparable to that of Pt, but the λ is about 4 times as much as that of Pt^{32,33}. Therefore, In₂Bi is a possible spin generator with higher spin current transport ability.

The terahertz (THz) emission spectroscopy is launched to systematically investigate the spin-to-charge conversion in In₂Bi besides electrical transport measurements. The mechanism of the THz emission is illustrated in Fig. 3d and Supplementary Note 4. The thickness of Co layer is fixed at 3 nm, while the In₂Bi layer thickness varies from 3 nm to 40 nm, as shown in Fig. 3e. We quantified the THz signal

amplitude by calculating the difference between the peak and valley values of their corresponding waveforms, as summarized in Table SI. The results demonstrate that the THz signal amplitudes of the Co/ In₂Bi heterojunction initially rises and then declines with the thickness of In₂Bi increasing. Notably, similar to the observations in SMR, the THz signal amplitude also peaks at the In₂Bi thickness of 13 nm.

To assess the THz measurements in Co/ In₂Bi bilayers, Co/Pt heterostructures are employed as comparison, which results are shown in Supplementary Note 5 and Fig. S6. The polarization of the THz waveforms for both Co/ In₂Bi and Co/Pt bilayers is the same, indicating that In₂Bi and Pt exhibit the same direction of spin current. Moreover, the THz polarization of Co (3)/W (3) stack shown in Fig. S7 further supports that the spin current direction of In₂Bi is consistent with Pt but opposite to W.

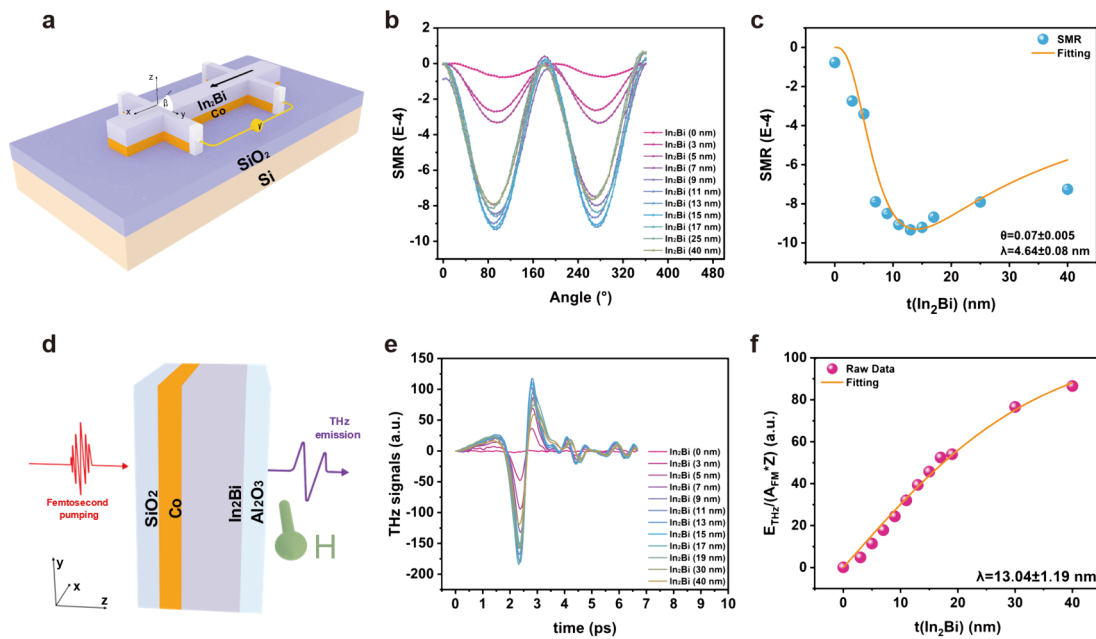


Fig. 3. The spin Hall magnetoresistance and THz emission measurement results of Co/In₂Bi heterostructures together with fitting curves. a, Schematic diagram of heterostructure

for spin Hall magnetoresistance measurement. **b**, Angle-dependent spin magnetoresistance curves of Co (3)/In₂Bi (t)/Al₂O₃ with varying In₂Bi thickness measured under 9 T at room temperature. **c**, Dependence of the SMR amplitude on the In₂Bi thickness in Co (3)/In₂Bi (t)/Al₂O₃ heterojunction and fitting curves. **d**, Schematic illustration of THz emission measurement geometry. The femtosecond laser propagates along z axis and a magnetic field is applied along x axis. **e**, THz signals for Co (3)/In₂Bi (t)/Al₂O₃ multilayers. **f**, The In₂Bi thickness dependence of the normalized THz amplitude for Co (3)/In₂Bi (t)/Al₂O₃ THz emitter. The symbol and line reveal the experimental and fitting results, respectively.

Fig. 3f depicts the relationship between THz signal amplitude and layer thickness for Co/In₂Bi/Al₂O₃ multilayers. To enable comparison, the impact of thickness variations on the laser absorption of FM layer (A_{FM}) and the THz emission impedance (Z) is evaluated. The theoretical fitting curve shown in Fig. 3f are derived from the following equation^{34, 35}:

$$E_{THZ} = A_{FM} \cdot Z \cdot G \cdot \theta_{SHE} \cdot \left[\tanh\left(\frac{t_N}{2\lambda}\right) \cdot \lambda \right]. \quad (2)$$

Here, E_{THZ} denotes the amplitude of the measured THz signals, A_{FM} is the laser absorption of the FM layer, Z is the THz radiation impedance, G is a parameter related to the generation and transmission of ultrafast spin current, and θ_{SHE} , λ , and t_N represent the spin Hall angle, the SDL and the thickness of the NM layer, respectively.

$A_{FM} = A_{total} \cdot \frac{t_F}{t_F + t_N}$, where A_{total} are the total laser absorbance of the bilayer, and t_{FM} is the thickness of the FM layer. By measuring the total laser absorbance, one can obtain A_{FM} . $Z = \frac{Z_0}{1 + n + Z_0 \cdot (\sigma_F t_F + \sigma_N t_N)}$, which can be obtained by measuring the THz

transmission of the sample and the bare substrate.

In equation (2), λ and $F \cdot \theta_{SHE}$ are adjustable parameters in fitting, while A and Z can be determined experimentally. The fitting curve presented in Fig. 3f reveals a strong consistency between the fitted and measured results³⁶. The fitting result indicates that In₂Bi has a long SDL of $\lambda_{\text{In}_2\text{Bi}}=13.04\pm 1.19$ nm. The SDL in Pt has also been studied and simulated to be 2.93 ± 0.24 nm (See Supplementary Note 5 and Fig. S6), which is consistent with previous reports^{37,38}. Furthermore, the $\lambda_{\text{In}_2\text{Bi}}$ is more than 4 times of λ_{Pt} according to THz measurements, which is in close agreement with the results from SMR tests. Although the absolute values of λ are different for SMR and THz fitting results due to the different mechanism^{33,35}, the ratio of $\lambda_{\text{In}_2\text{Bi}}/\lambda_{\text{Pt}}$ obtained from the same method can reflect the capability of spin transport of materials. Therefore, In₂Bi possesses a significant long SDL comparing to transition metals with strong SOC, which is beneficial for In₂Bi as a spin generator.

DFT calculations

To further investigate the origin of large SHA and long SDL in hexagonal In₂Bi, we perform first-principles calculations. The In₂Bi crystal has a hexagonal P6₃/mmc space group (No. 194) with lattice parameters $a = b = 5.559$ Å and $c = 6.508$ Å (Fig. 4a), and its Brillouin zone is shown in Fig. 4b. The schematic and calculated band structures in the absence and presence of SOC are shown in Fig. 4c and 4d, respectively. The density of state (DOS) results confirms the significant contribution of p-orbital electrons to the electronic transport properties (Fig. 4e). As a semimetal, In₂Bi exhibits

a relatively low DOS near the Fermi level, where the conduction and valence bands are entangled, leading to numerous band-crossing structures. Under the influence of SOC, these band crossings are degenerated, giving rise to many spin Berry curvature (SBC) hotspots as shown in Fig. 4f by the color changes with opposite signs. Several band-crossings occur within the energy range of ± 0.5 eV, stabilizing the nonzero components of spin Hall conductivity (SHC) (Fig. 4g). The integral SBC of occupied states along high-symmetry paths (Fig. 4h) reveals a maximum and a minimum near the Γ -point and H-point, respectively, perfectly aligning with the SBC hotspots at the corresponding locations in Fig. 4f. Additionally, other hotspot regions in Fig. 4f are also reflected as local peak variations in Fig. 4h.

The SHA is defined by the ratio of the SHC to the longitudinal electrical conductivity (EC), i.e. $\theta_{SH} = \frac{2e}{h} \left| \frac{\sigma_{xy}^z}{\sigma_{xx}} \right|$ is the SHA for σ_{xy}^z , which shows great importance of EC influencing on the magnitude of SHA. σ_{xy}^z describes the spin current J_s in x direction with spin polarization along z direction due to an incoming charge current from the y direction. We further determined the EC of In₂Bi with considering electron-phonon scattering and analyzed the temperature-dependent variations of both EC and SHC, as shown in Fig. 4i. The calculated SHC of In₂Bi is approximately 65% that of Pt³⁹. However, as a semimetal, In₂Bi exhibits relatively low electrical conductivity (with a theoretical EC value only one-fifth that of Pt⁴⁰). This combination results in a theoretical SHA for In₂Bi of 0.15 at room temperature, which is about two times as much as that of Pt⁴¹.

In our experiments, the observed SHA is similar to that of Pt, which may be due to

the orientation of the crystal during the preparation of the film. The XRD and TEM analysis reveal that there are two dominated (102) and (110) planes in the In₂Bi layer. To investigate the impact of crystal orientation on the SHA, we calculate the SHC of different planes (Supplementary Note 6, Fig. S8 and Fig. S9), where the σ_{xy}^z of (102) and (110) planes are around 517 and 674 $\hbar/e(S/cm)$, respectively, which show a decrease of more than 50% compared with the bulk material. This is in good agreement with the observed SHA in experiments.

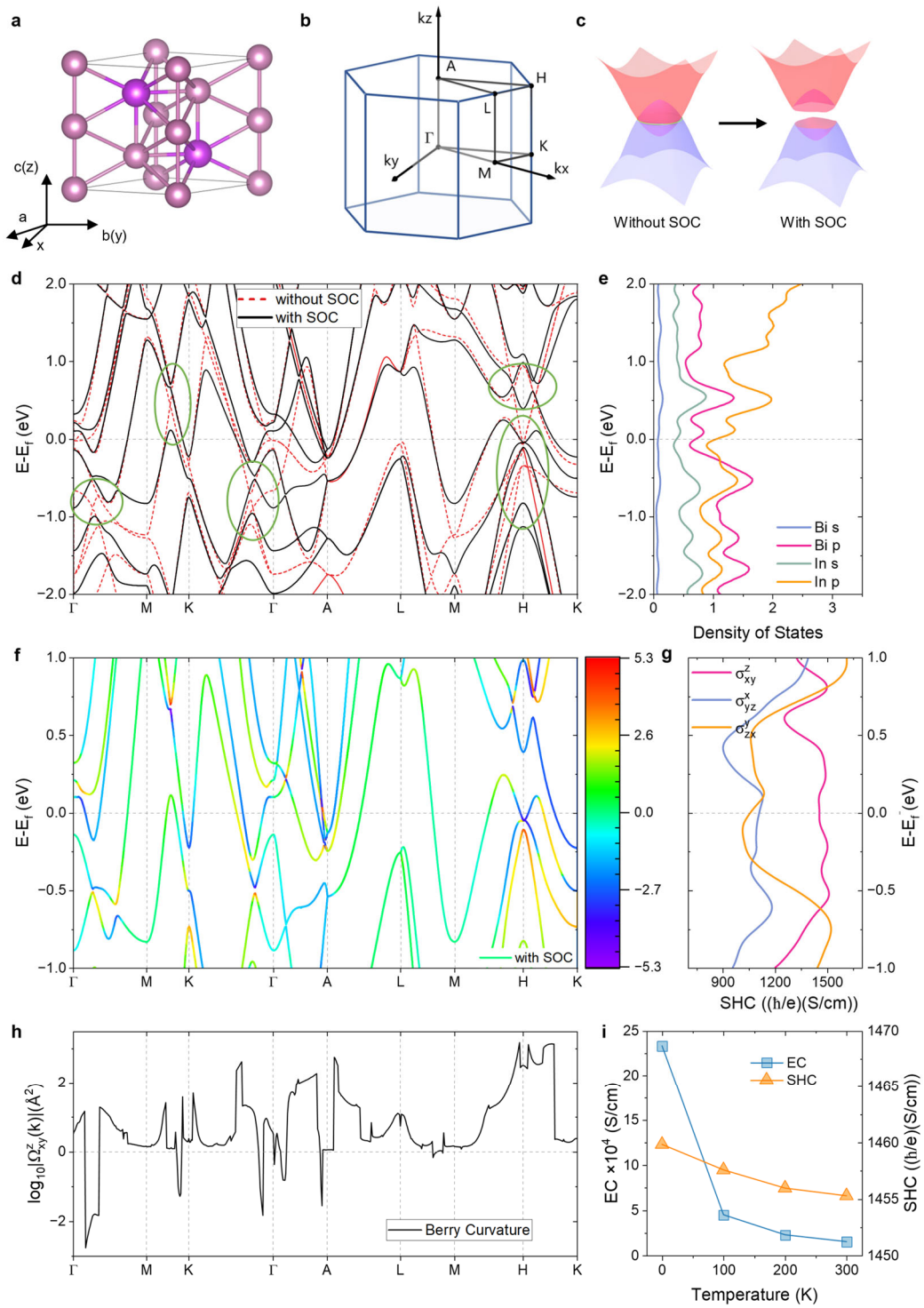


Fig. 4. Crystal and electronic structures of In_2Bi as well as the spin Hall conductivity, electrical conductivity and spin Berry curvature. **a**, In_2Bi crystal structure with space group $P6_3/mmc$ (194). The a , b , c are the crystal-axis directions. **b**, Brillouin zone for In_2Bi . **c**, Schematic of the band

splitting under the SOC effect in a large spin Berry curvature along the original nodal line, and further contributes to large SHC. **d**, The calculated band structures along the high symmetry directions with (black) and without (red) SOC. The green circles highlight Weyl points and their opening gaps by SOC near the Fermi level. **e**, The projected density of states. **f**, The band structure of In₂Bi projected by spin Berry curvature of Ω_{xy}^z . **g**, Three nonzero tensor elements of SHC plotted as a function of energy. **h**, The k-resolved spin Berry curvatures of Ω_{xy}^z on a log scale. **i**, The temperature dependence of spin Hall conductivity (orange) and electrical conductivity (blue) at the Fermi energy.

Conclusion and outlook

Based on the experimental and theoretical results, due to the large Berry curvature and the relatively low basic conductivity, In₂Bi possesses a large spin Hall angle and a long spin diffusion length, which makes it capable of efficient charge-to-spin conversion. As illustrated in Fig. 1a, traditional d-orbital spin current source materials, such as heavy metals, depend on the strong SOC originating from 5d elements. Such strong SOC contributes to the large SHA. However, the localized DOS of d-orbital and the large scattering by strong SOC lead to a small SDL, confining the spin current propagation. To overcome such a dilemma in d-orbital metals, we demonstrate that In₂Bi, an IIIA-VA group p-orbital alloy exhibits both large SHC and long SDL (Fig. 1b). This is due to the large Berry curvature and the delocalized character of the p-orbital, which facilitate the propagation of spin currents. Therefore, p-orbital materials like the In₂Bi alloy can also serve in charge-to-spin conversion, breaking the limitation of conventional 5d heavy materials. This work offers not only a route to enhance spin

current efficiency but also expanding the range of materials applicable to spintronic devices.

Reference

1. M. C. Beeler *et al.*, The spin Hall effect in a quantum gas. *Nature* **498**, 201-204 (2013).
2. I. A. Ado, A. Qaiumzadeh, R. A. Duine, A. Brataas, M. Titov, Asymmetric and Symmetric Exchange in a Generalized 2D Rashba Ferromagnet. *Phys. Rev. Lett.* **121**, 086802 (2018).
3. Z. G. Yu, Spin-Orbit Coupling, Spin Relaxation, and Spin Diffusion in Organic Solids. *Phys. Rev. Lett.* **106**, 106602 (2011).
4. R. Nakajima, *et al.*, Giant spin polarization and a pair of antiparallel spins in a chiral superconductor. *Nature* **613**, 943-945 (2023).
5. Z. Y. Zhou *et al.*, Manipulation of the altermagnetic order in CrSb via crystal symmetry. *Nature* **638**, 645-650 (2019).
6. Y. Fan *et al.*, Magnetization switching through giant spin-orbit torque in a magnetically doped topological insulator heterostructure. *Nat. Mater.* **13**, 699-704 (2014).
7. H. Wang *et al.*, Room temperature energy-efficient spin-orbit torque switching in two-dimensional van der Waals Fe₃GeTe₂ induced by topological insulators. *Nat. Commun.* **14**, 5173 (2023).
8. L. You *et al.*, Switching of perpendicularly polarized nanomagnets with spin orbit torque without an external magnetic field by engineering a tilted anisotropy. *Proceedings of the National Academy of Sciences* **112**, 10310-10315 (2015).
9. C. H. Jin *et al.*, Imaging of pure spin-valley diffusion current in WS₂/WSe₂ heterostructures. *Science* **360**, 893-896 (2018).
10. P. Vaidya *et al.*, Subterahertz spin pumping from an insulating antiferromagnet. *Science* **368**, 160-165 (2020).
11. A. Manchon *et al.*, Current-induced spin-orbit torques in ferromagnetic and antiferromagnetic systems. *Reviews of Modern Physics* **91**, 035004 (2019).
12. M. Dc *et al.*, Room-temperature high spin-orbit torque due to quantum confinement in sputtered Bi_xSe_(1-x) films. *Nat. Mater.* **17**, 800-807 (2018).
13. J. X. Li *et al.*, Spin current from sub-terahertz-generated antiferromagnetic magnons. *Nature* **578**, 70-74 (2020).
14. R. Yu *et al.*, Determination of spin Hall angle and spin diffusion length in β -phase-dominated tantalum. *Physical Review Materials* **2**, 074406 (2018).
15. J. Kim, P. Sheng, S. Takahashi, S. Mitani, M. Hayashi, Spin Hall Magnetoresistance in Metallic Bilayers. *Phys. Rev. Lett.* **116**, 097201 (2016).
16. P. Sheng *et al.*, The spin Nernst effect in tungsten. *Science advances* **3**, e1701503 (2017).
17. E.-S. Park *et al.*, Strong higher-order angular dependence of spin-orbit torque in W/CoFeB bilayer. *Physical Review B* **107**, 064411 (2023).
18. Y. Li *et al.*, Enhancing the Spin-Orbit Torque Efficiency by the Insertion of a Sub-nanometer β -W Layer. *ACS Nano* **16**, 11852-11861 (2022).
19. J. W. Lee *et al.*, Enhanced spin-orbit torque by engineering Pt resistivity in Pt/Co/AIO structures. *Physical Review B* **96**, 064405 (2017).
20. M. Fang *et al.*, Tuning the interfacial spin-orbit coupling with ferroelectricity. *Nat. Commun.* **11**, 2627 (2020).
21. M. Isasa, E. Villamor, L. E. Hueso, M. Gradhand, F. Casanova, Temperature dependence of spin diffusion length and spin Hall angle in Au and Pt. *Physical Review B* **91**, 024402 (2015).

22. X. K. Xu *et al.*, Giant Extrinsic Spin Hall Effect in Platinum-Titanium Oxide Nanocomposite Films. *Advanced Science* **9**, 9 (2022).
23. M. V. Berry, Quantal phase factors accompanying adiabatic changes. *Proceedings of the Royal Society of London. A. Mathematical Physical Sciences* **392**, 45-57 (1984).
24. C. L. Kane, E. J. Mele, Quantum Spin Hall Effect in Graphene. *Phys. Rev. Lett.* **95**, 226801 (2005).
25. D. J. Thouless, M. Kohmoto, M. P. Nightingale, M. den Nijs, Quantized Hall Conductance in a Two-Dimensional Periodic Potential. *Phys. Rev. Lett.* **49**, 405-408 (1982).
26. D. Xiao, M.-C. Chang, Q. Niu, Berry phase effects on electronic properties. *Reviews of Modern Physics* **82**, 1959-2007 (2010).
27. Y. Zhang *et al.*, Different types of spin currents in the comprehensive materials database of nonmagnetic spin Hall effect. *npj Computational Materials* **7**, 167 (2021).
28. F. Schindler *et al.*, Higher-order topology in bismuth. *Nat. Phys.* **14**, 918-924 (2018).
29. R. Noguchi *et al.*, Evidence for a higher-order topological insulator in a three-dimensional material built from van der Waals stacking of bismuth-halide chains. *Nat. Mater.* **20**, 473-479 (2021).
30. Y. Lu *et al.*, Topological Properties Determined by Atomic Buckling in Self-Assembled Ultrathin Bi(110). *Nano Lett.* **15**, 80-87 (2015).
31. Y. Zhang *et al.*, Spin Nernst effect in a p-band semimetal InBi. *New Journal of Physics* **22**, 093003 (2020).
32. M.-H. Nguyen, D. C. Ralph, R. A. Buhrman, Spin Torque Study of the Spin Hall Conductivity and Spin Diffusion Length in Platinum Thin Films with Varying Resistivity. *Phys. Rev. Lett.* **116**, 126601 (2016).
33. Y. Wang, P. Deorani, X. Qiu, J. H. Kwon, H. Yang, Determination of intrinsic spin Hall angle in Pt. *Appl. Phys. Lett.* **105**, 152412 (2014).
34. P. Wang *et al.*, Inverse orbital Hall effect and orbitronic terahertz emission observed in the materials with weak spin-orbit coupling. *npj Quantum Materials* **8**, 28 (2023).
35. H. Zhang *et al.*, Laser pulse induced efficient terahertz emission from Co/Al heterostructures. *Physical Review B* **102**, 024435 (2020).
36. L. Zhu, D. C. Ralph, R. A. Buhrman, Highly Efficient Spin-Current Generation by the Spin Hall Effect in Au(1-x)P(x). *Physical Review Applied* **10**, 031001 (2018).
37. M. Kawaguchi, D. Towa, Y.-C. Lau, S. Takahashi, M. Hayashi, Anomalous spin Hall magnetoresistance in Pt/Co bilayers. *Appl. Phys. Lett.* **112**, 152412 (2018).
38. J. Qin, D. Hou, Y. Chen, E. Saitoh, X. Jin, Spin Hall magnetoresistance in Pt/Cr₂O₃/YIG structure. *J. Magn. Magn. Mater.* **534**, 167980 (2021).
39. J. Qiao, J. Zhou, Z. Yuan, W. Zhao, Calculation of intrinsic spin Hall conductivity by Wannier interpolation. *Physical Review B* **98**, 214402 (2018).
40. X. Zhang, S. Li, A. Wang, H. Bao, Pressure-dependent thermal conductivity in Al, W, and Pt: Role of electrons and phonons. *Physical Review B* **106**, 094313 (2022).
41. Y. Wang, P. Deorani, X. Qiu, J. H. Kwon, H. Yang, Determination of intrinsic spin Hall angle in Pt. *Applied Physics Letters* **105**, 152412 (2014).

Methods

Magnetron sputtering

Magnetron sputtering leverages the interplay between magnetic and electric fields to exert precise control over plasma dynamics, effectively enhancing both the sputtering rate and film quality. Based on the principles of physical vapor deposition (PVD), magnetron sputtering relies on high-energy ions to bombard the target material, resulting in the ejection of atoms from the target surface, which then deposit onto a substrate to form a thin film.

The base pressure for thin film deposition was maintained at 9×10^{-6} Pa. For the deposition of the In₂Bi layer, sputtering was performed at an Ar pressure of 0.6 Pa with a DC power of 4 W. Co was sputtered at the same pressure (0.6 Pa) with a DC power of 40 W. For Pt, sputtering was carried out at an Ar pressure of 0.4 Pa with a DC power of 15 W. Al₂O₃ was deposited at an Ar pressure of 0.8 Pa using RF power set to 50 W.

Terahertz emission

In this study, we employed a standard THz time-domain spectroscopy setup to generate and detect THz pulse waveforms. A linearly polarized femtosecond laser pulse (120 fs duration, 800 nm central wavelength, 500 mW (P_{in}), 80 MHz repetition rate) was incident on the thin film along the z-axis. A magnetic field of 0.1 T (B) was applied along the x-axis to orient the magnetization of the ferromagnetic layer. The THz signal, characterized by an electric field oriented along the y-axis, was emitted from the device and detected by a photoconductive antenna. All measurements were conducted in a dry air environment at room temperature. In principle, either side of the sample can be

pumped—either the substrate side or the ferromagnetic layer side. However, in the current experiment, pumping was performed from the substrate side to mitigate undesired THz absorption by the substrate, thereby facilitating THz emission from the surface of the thin film.

DFT calculations

The first-principles calculations are carried out with QUANTUM ESPRESSO⁴²,⁴³. Before calculation, the structure was fully relaxed with the force on each atom was less than 10^{-3} Ry/Bohr. In order to calculate the spin hall conductivity (SHC), a plane-wave basis was used and the pseudopotential was from PSLIBRARY⁴⁴. We used a fully relativistic pseudopotential with the generalized gradient approximation (GGA) based on the projector wave augmented (PAW) method with a Perdew-Burke-Ernzerhof (PBE) functional. The plane-wave and charge-density cutoff energy are 80 Ry and 400 Ry, respectively. A k-point grid of $10 \times 10 \times 10$ was used in the self-consistent calculations. Spin-orbit interaction was taken into account self-consistently, which also includes scalar relativistic effects. Once the self-consistent calculations were completed, the Bloch functions were Fourier transformed to the maximally localized Wannier functions (MLWFs) using the WANNIER90 package⁴⁵. The chosen Wannier functions are In: s, d, Bi: s, p. After the k-point grid convergence test and method comparison (Supplementary Note 7), the WannierBerri algorithm considering material crystal symmetry can converge to an accurate result under relatively coarse k-mesh with shorter calculation time. Therefore, the calculation method from Qiao et al.⁴⁶ integrated in the Wannierberri package⁴⁷ was used to complete subsequent calculations. The SHC

of bulk In₂Bi was calculated on a dense $100 \times 100 \times 100$ k-mesh while for the structure of In₂Bi in different phase, it was calculated on a relatively coarse $50 \times 50 \times 50$ k-mesh using WannierBerri.

In order to evaluate the electrical conductivity (EC), the energy and k-point dependent carrier relaxation time is calculated by utilizing EPW package⁴⁸. Since the SOC has little effect on the force constants and phonon frequencies, we employ norm-conversing pseudopotentials⁴⁹ with the Perdew-Burke-Ernzerhof (PBE) form of the exchange-correlation functional for electrical conductivity calculation. The cutoff energy of the plane wave is set as 80 Ry, while the convergence threshold of electron energy is set to be 10^{-12} Ry for the self-consistent field calculation. The phonon dispersion relations are calculated by density functional perturbation theory⁵⁰, with a $6 \times 6 \times 6$ q grid and a self-consistency threshold of 10^{-14} . Using the maximally localized Wannier functions basis⁵¹, the electron-phonon matrix elements, band energies, and phonon modes are interpolated from an initial coarse grid of $12 \times 12 \times 12$ and $6 \times 6 \times 6$ electron and phonon vector grids, respectively, to dense grids of $60 \times 60 \times 60$ and $40 \times 40 \times 40$ electron and phonon vector grids, respectively.

Acknowledgements

X.G.X. acknowledges the financial support from the National Key R&D Program of China (2022YFA1402602) and National Natural Science Foundation of China (Grant Nos. U24A6001, U24A6002 and U23A20548). L.S. acknowledges the financial support from Singapore MOE Tier 1 (No. A-8001194-00-00) and Singapore MOE Tier 2 (No. A-8001872-00-00). Z.F. acknowledges the financial support from National

Natural Science Foundation of China (Grant No. 62027807).

Author contributions:

X.G.X. and L.S. conceived the project and designed the experiments; G.L. and Y.Z. wrote the manuscript; G.L. performed heterostructure growth, device fabrication, material characterization, and SMR measurements under the supervision of X.G.X., K.K.M., Y.W. and Y.J.; Y.Z. performed the calculations and theoretical analysis under the supervision of L.S. and Y.H.W.; Z.F., K.H. and W.T. performed the THz measurement and analyzed the results; A.L. helped in TEM characterization; L.C. helped in SMR measurement and device fabrication. All authors discussed and analyzed the results and commented on the manuscript.

Competing interests:

The authors declare that they have no competing interests.

Data and materials availability:

All data are available in the main text or the Supplementary Materials.

Additional information

Supplementary Information is available for this paper.

Correspondence and requests for materials should be addressed to Xiaoguang Xu,

Lei Shen and Yong Jiang.

Supplementary Materials for

Observation of charge to spin conversion in p-orbital InBi alloy

Gen Li[†], Ying Zhang[†], Xiaoguang Xu^{*}, Lei Shen^{*}, Zheng Feng, Kangkang Meng, Ang Li, Lu Cheng, Kang He, Wei Tan, Yong Wu, Yihong Wu, Yong Jiang^{*}

Corresponding author. xgxu@ustb.edu.cn (X.G.X.); shenlei@nus.edu.sg (L.S.);
yjiang@ustb.edu.cn (Y.J.)

Note 1. Phase analysis and surface morphology of In₂Bi

Note 2: The mechanism of spin Hall magnetoresistance

Note 3: SMR fitting of In₂Bi film with different thickness

Note 4: THz emission test mechanism

Note 5: THz emission test of Co/Pt heterostructure

Note 6: Crystal structure and SHC of In₂Bi in phase (102) and (110)

Note 7: Method comparison and k-mesh converge test

Note1: Phase analysis and surface morphology of In₂Bi

The peak areas of XPS spectrum corresponding to In and Bi can be integrated and, using the sensitivity factors (S) for the respective elements, the concentration ratio can be calculated as follows:

$$n_i / n_j = (I_i / S_i) / (I_j / S_j)$$

where $n_{i/j}$, $I_{i/j}$ and $S_{i/j}$ represent the element concentrations, corresponding peak areas, and sensitivity factors, respectively

By accounting for sensitivity factors and integrating the peak intensities, the surface atomic ratio of In/Bi is estimated to be approximately 2.54 using In 3d and Bi 4f orbitals. This value slightly exceeds the target stoichiometry. However, XPS provides only semi-quantitative estimates of atomic ratios. More precise and comprehensive measurement techniques are necessary for an accurate determination of the In/Bi ratio. The intensity ratio of In $d_{5/2}$ to $d_{3/2}$ is approximately 1.527, while the ratio of Bi $f_{7/2}$ to $f_{5/2}$ is about 1.319, aligning with the expected 3:2 and 4:3 ratios for d and f orbitals, respectively. The Bi 4p and In 3p orbitals, as well as the Bi 4d and In 3d orbitals, are shown in Figs. S3a and S3b, respectively.

In order to accurately measure the atomic ratio, inductively coupled plasma optical emission spectrometer (ICP-OES) measurement was employed and demonstrates a precise In/Bi atomic concentration ratio of 2:1, confirming that the resulting In₂Bi films exhibit the desired stoichiometry.

Note 2: The mechanism of spin Hall magnetoresistance

In SMR testing, both the spin Hall effect (SHE) and the inverse spin Hall effect (ISHE) operate simultaneously. The SHE converts electrical currents into transverse spin currents, while the angle between the spin polarization direction in the non-magnetic layer and the magnetization direction of the adjacent ferromagnetic layer determines whether the spin current is absorbed or reflected. Reflected spin currents are subsequently converted back into charge currents through ISHE, leading to changes in the magnetoresistance (MR).

In this configuration, Co acts as the ferromagnetic layer (FM), In₂Bi as the non-magnetic layer (NM), and Al₂O₃ as the capping layer. The SHE in In₂Bi induces a spin current J_s , which propagates perpendicularly to the film surface with a spin polarization direction parallel to the interface. As the device rotates in the yz-plane, the magnetization M remains aligned with the external magnetic field. When the spin polarization and M are not collinear, a portion of the spin current is absorbed by the magnetization at the NM/FM interface, while another portion is reflected and reconverted into charge current via ISHE. When M is parallel to the spin polarization, absorption is zero, resulting in maximum J_e . When M is perpendicular to the spin polarization, spin current is absorbed by FM layer, corresponding to minimum J_e . Thus, the direction of magnetization in Co affects the resistance of the In₂Bi film, yielding SMR.

Note3: SMR fitting of In₂Bi film with different thickness

We performed SMR measurements on Co (3 nm)/ In₂Bi (t nm) heterostructures, with In₂Bi layer thicknesses of t = 0, 3, 5, 7, 9, 11, 13, 15, 17, 25, and 40 nm. When the spin polarization in the In₂Bi layer is parallel to the magnetization of the Co layer, spin current is reflected at the interface and reconverted into charge current via the ISHE in the In₂Bi layer. This additional charge current adds to the original longitudinal charge current, resulting in a low-resistance state. Conversely, when the spin polarization is perpendicular to the magnetization, the spin current is absorbed by the Co layer at the interface, suppressing reflection and leading to a reduced contribution to the longitudinal current, manifesting as a high-resistance state.

The SMR can be described by the following relationship:

$$\rho_{xx} = \rho_0 + \Delta\rho_{xx}[\hat{m} \cdot (\hat{j} \times \hat{z})]^2 \quad (\text{S1})$$

where ρ_0 is the normal resistivity, ρ_{xx} is the amplitude of the SMR, and \hat{m} 、 \hat{j} 、 \hat{z} represent the magnetization, current direction, and the vector normal to the interface, respectively.

In the y-z plane, as the magnetization rotates under the external magnetic field, it remains perpendicular to the current direction. Thus, anisotropic magnetoresistance (AMR) has no contribution to MR, and only SMR is taken into account. The angular dependence of SMR, observed as the magnetic field rotates in the plane, is depicted in Fig S5.

Note 4: THz emission test mechanism

The granular nature of the In₂Bi film may influence conventional electrical transport measurements. Consequently, an alternative characterization method is necessary to validate the spin currents generated in In₂Bi, separate from traditional electrical transport testing. The ISHE has recently emerged as a pivotal factor in extending the field of spintronics into the terahertz (THz) domain (52). THz spintronics holds considerable promise for applications in high-speed currents and computing technologies (53). Therefore, THz emission test was used to further verify the spin current in In₂Bi. In the context of THz emission induced by ISHE in ferromagnetic/non-magnetic (FM/NM) layers, a femtosecond laser pulse pumps the FM/NM heterostructure, generating non-equilibrium spin-polarized electrons within the FM layer. These electrons subsequently diffuse through the non-magnetic layer via super diffusion (54,55). Due to ISHE in the NM layer, the spin current is converted into a transient transverse charge current, which produces short THz pulses that propagate perpendicularly to the current direction.

Note 5: THz emission test of Co/Pt heterostructure

Co/Pt heterostructures were obtained under the same experimental conditions as those employed for the Co/In₂Bi stack. Co (3 nm)/Pt (t nm) heterostructures (where t = 0, 1, 2, 3, 4, 5, 7, 10, 13 and 16 nm) are fabricated and conducted THz measurements. Just like Co/In₂Bi samples, the signal strength is quantified as the difference between the amplitudes of peaks and troughs. The results were obtained under the same experimental conditions as those employed for the Co/In₂Bi stack. The signal strength reached a peak of approximately 900. The results demonstrate that as the thickness of Pt increases, the signal strength in the Co/Pt heterojunction initially rises and then declines. Similar to the observations in SMR, the THz intensity also reach peaks at the Pt thickness reaches 2-3 nm. The fitting results indicate that $\lambda_{Pt}=2.93\pm 0.24$ nm.

Note 6: Crystal structure and SHC of In₂Bi in phase (102) and (110)

In order to analyze the SHC of In₂Bi in different phases, we construct In₂Bi structures in phases (102) and (110), and took 4 and 6 layers of atoms as examples to simulate the actual performance of In₂Bi materials under experimental conditions. To facilitate analysis, we listed the complete SHC tensor of bulk In₂Bi and bulk Pt for comparison.

The SHC tensor of bulk In₂Bi at fermi energy¹:

$$\begin{aligned} \sigma^x &= \begin{pmatrix} 0 & 0 & 0 \\ 0 & 0 & -1058.11 \\ 0 & 1109.90 & 0 \end{pmatrix} (\hbar/e(S/cm)) \\ \sigma^y &= \begin{pmatrix} 0 & 0 & 1058.59 \\ 0 & 0 & 0 \\ -1110.38 & 0 & 0 \end{pmatrix} (\hbar/e(S/cm)) \\ \sigma^z &= \begin{pmatrix} 0 & -1456.13 & 0 \\ 1455.27 & 0 & 0 \\ 0 & 0 & 0 \end{pmatrix} (\hbar/e(S/cm)) \end{aligned}$$

The SHC tensor of bulk Pt at fermi energy¹:

$$\begin{aligned} \sigma^x &= \begin{pmatrix} 0 & 0 & 0 \\ 0 & 0 & -2234.81 \\ 0 & 2234.81 & 0 \end{pmatrix} (\hbar/e(S/cm)) \\ \sigma^y &= \begin{pmatrix} 0 & 0 & 2234.81 \\ 0 & 0 & 0 \\ -2234.81 & 0 & 0 \end{pmatrix} (\hbar/e(S/cm)) \\ \sigma^z &= \begin{pmatrix} 0 & -2234.81 & 0 \\ 2234.81 & 0 & 0 \\ 0 & 0 & 0 \end{pmatrix} (\hbar/e(S/cm)) \end{aligned}$$

Extensive studies have shown that the crystal phase of the protected nodal lines contribute significantly to the larger SHC (27, 37), so the symmetry of the structure in different phases are fully analyzed. Protected by six-fold symmetry and multiple crystal plane symmetry, the original In₂Bi lattice has 24 symmetric operations, while the In₂Bi of (102) retains only one mirror symmetry plane. The overall lattice structure presents a high degree of disorder, resulting in a significant decline in the calculated SHC (Fig.

S8). Symmetry breaking results in the appearance of more than three non-zero components in the SHC tensor. Although the positions of these non-zero terms in the tensor show a regular arrangement, there is no inverse sign phenomenon consistent with the bulk structure.

SHC tensor for In₂Bi in (102) phase with 4-atom-layer at fermi energy¹:

$$\begin{aligned} \sigma^x &= \begin{pmatrix} 0 & 57.69 & 0 \\ 64.44 & 0 & 8.80 \\ 0 & 40.63 & 0 \end{pmatrix} (\hbar/e(S/cm)) \\ \sigma^y &= \begin{pmatrix} -55.09 & 0 & 31.39 \\ 0 & 147.42 & 0 \\ -32.73 & 0 & 5.37 \end{pmatrix} (\hbar/e(S/cm)) \\ \sigma^z &= \begin{pmatrix} 0 & -276.29 & 0 \\ 281.14 & 0 & 7.57 \\ 0 & -1.89 & 0 \end{pmatrix} (\hbar/e(S/cm)) \end{aligned}$$

SHC tensor for In₂Bi in (102) phase with 6-atom-layer at fermi energy¹:

$$\begin{aligned} \sigma^x &= \begin{pmatrix} 0 & -58.83 & 0 \\ 130.07 & 0 & -76.46 \\ 0 & 77.56 & 0 \end{pmatrix} (\hbar/e(S/cm)) \\ \sigma^y &= \begin{pmatrix} -62.18 & 0 & 136.68 \\ 0 & 7.75 & 0 \\ -69.94 & 0 & 3.67 \end{pmatrix} (\hbar/e(S/cm)) \\ \sigma^z &= \begin{pmatrix} 0 & -353.61 & 0 \\ 516.58 & 0 & -120.88 \\ 0 & 9.36 & 0 \end{pmatrix} (\hbar/e(S/cm)) \end{aligned}$$

As for the In₂Bi in (110) phase (Fig. S9), the symmetry of the original In₂Bi structure is more preserved, thus retaining relatively higher SHC than (102) phase. Compared with the 4-atom-layer structure, the 6-atom-layer structure is closer to the actual bulk structure, so the calculated results are closer to the value of the bulk system. In addition, the preservation of symmetry is also reflected in the SHC tensor. The tensor on the (110) plane maintains consistency with the original bulk structure, as evidenced by the number, positions, and directional relationships of its non-zero components aligning with those of the bulk. However, due to the reduction of symmetry, the inverse sign relationship between the elements is not fully preserved. The construction of the cleaved plane reduces the spin polarization components along the x and y directions to

¹ For each element in SHC tensor, the superscripts denote the spin polarization direction, while the subscripts represent the current direction and spin current direction, respectively.

one-tenth of their bulk values, while the z-direction component is approximately halved.

SHC tensor for In₂Bi in (110) phase with 4-atom-layer at fermi energy¹:

$$\begin{aligned} \sigma^x &= \begin{pmatrix} 0 & 0 & 0 \\ 0 & 0 & -87.54 \\ 0 & 78.64 & 0 \end{pmatrix} (\hbar/e(S/cm)) \\ \sigma^y &= \begin{pmatrix} 0 & 0 & 64.46 \\ 0 & 0 & 0 \\ -89.85 & 0 & 0 \end{pmatrix} (\hbar/e(S/cm)) \\ \sigma^z &= \begin{pmatrix} 0 & -488.81 & 0 \\ 799.62 & 0 & 0 \\ 0 & 0 & 0 \end{pmatrix} (\hbar/e(S/cm)) \end{aligned}$$

SHC tensor for In₂Bi in (110) phase with 6-atom-layer at fermi energy¹:

$$\begin{aligned} \sigma^x &= \begin{pmatrix} 0 & 0 & 0 \\ 0 & 0 & -179.97 \\ 0 & 133.05 & 0 \end{pmatrix} (\hbar/e(S/cm)) \\ \sigma^y &= \begin{pmatrix} 0 & 0 & 174.00 \\ 0 & 0 & 0 \\ -153.66 & 0 & 0 \end{pmatrix} (\hbar/e(S/cm)) \\ \sigma^z &= \begin{pmatrix} 0 & -742.97 & 0 \\ 674.18 & 0 & 0 \\ 0 & 0 & 0 \end{pmatrix} (\hbar/e(S/cm)) \end{aligned}$$

Note 7: Method comparison and k-mesh converge test

In order to obtain more accurate SHC calculation results while taking into account the computational amount, we take the σ_{xy}^z component of SHC for In₂Bi block material as an example to test the calculation performance of Wannier90 and WannierBerri in different k-point grids (Fig. S10). With the increase of the k-point grid, the calculated values of the two methods gradually tend to the same curve, which reflects the consistency of the results under different algorithms. The calculation accuracy and calculation speed of Wannier90 are greatly affected by the k-point grid. The coarser grid makes the results more volatile and significantly underestimates the value, while the denser grid will significantly increase the calculation time. WannierBerri leverages the symmetry properties of crystals, requiring only irreducible k-points for computation. This approach significantly reduces the computational workload. Aside from noticeable fluctuations in results when the k-point mesh size is set to 30, the calculations demonstrate high consistency with further increases in the k-point density.

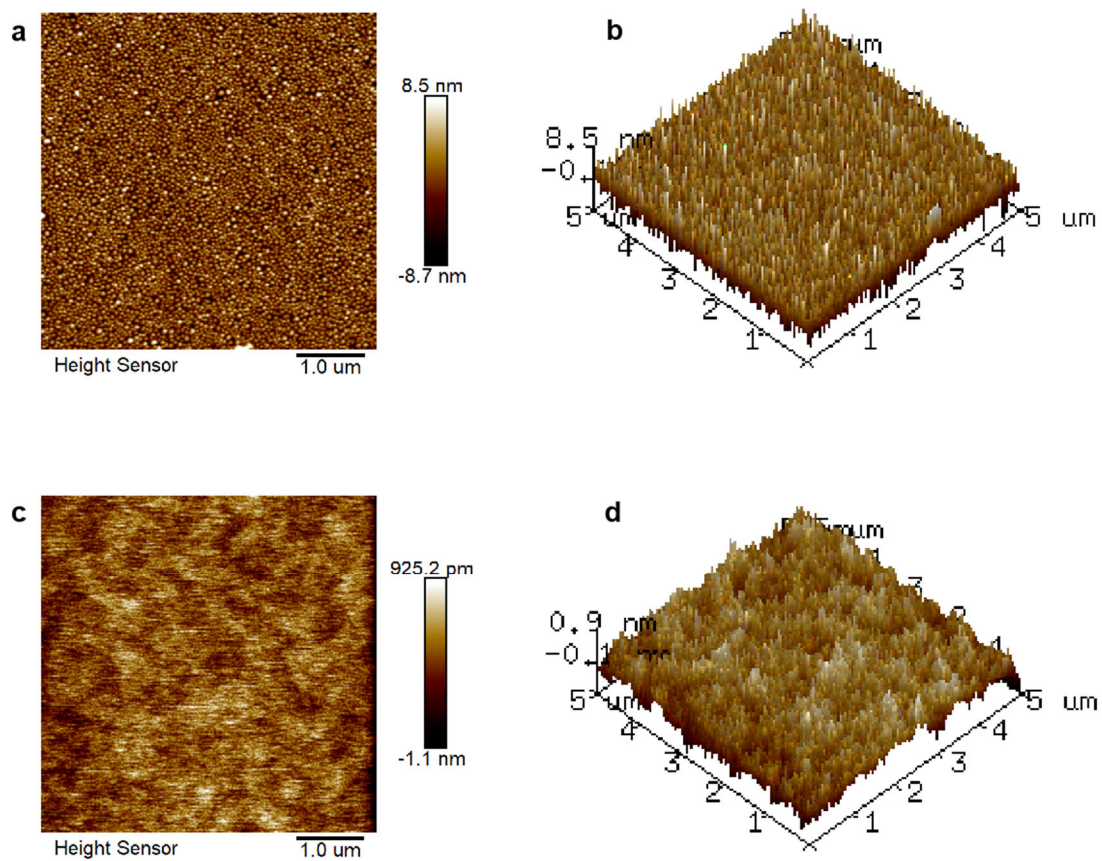


Fig. S1 a, 2D and b, 3D images of a 13 nm In_2Bi film with a roughness R_q of ~ 2.5 nm. c, 2D and d, 3D images of a 3 nm Co film with a roughness R_q of ~ 0.28 nm.

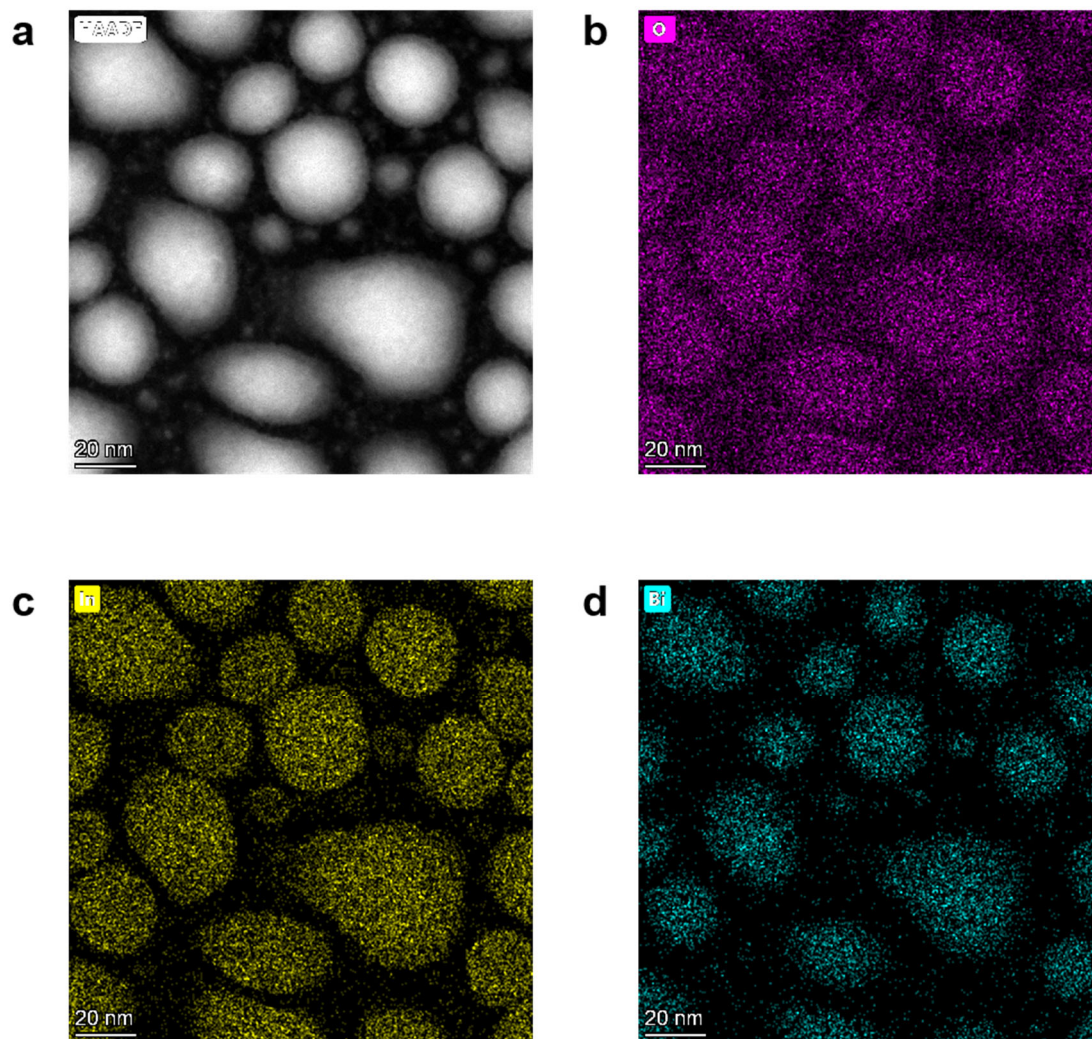


Fig. S2. a, HAADF image of a 13 nm In_2Bi . EDS mapping images of b, In, c, Bi and d, O in In_2Bi grown on SiN substrates.

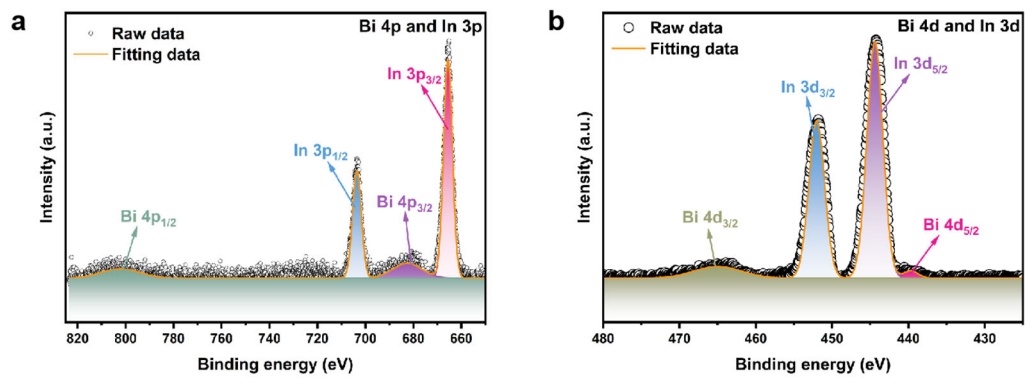


Fig. S3. a, XPS spectra of Bi 4p and In 3p orbitals. **b**, XPS spectra of Bi 4d and In 3d orbitals.

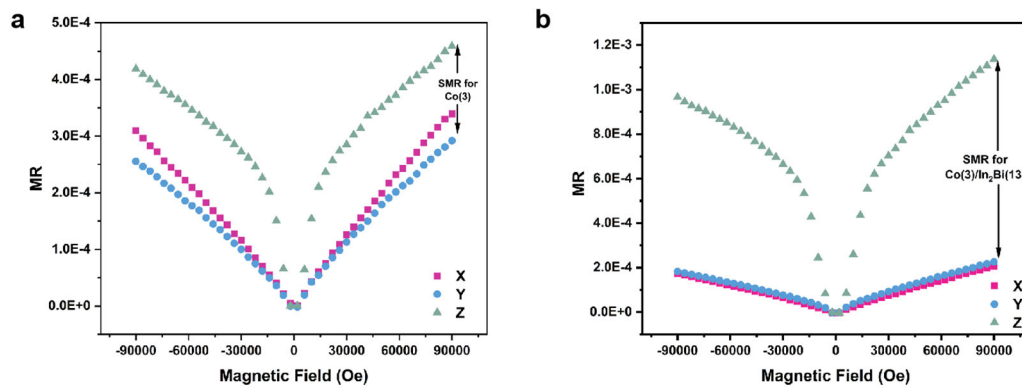


Fig. S4. Scan field Magnetoresistance in X, Y and Z direction of **a**, Co (3) and **b**, Co (3)/In₂Bi (13).

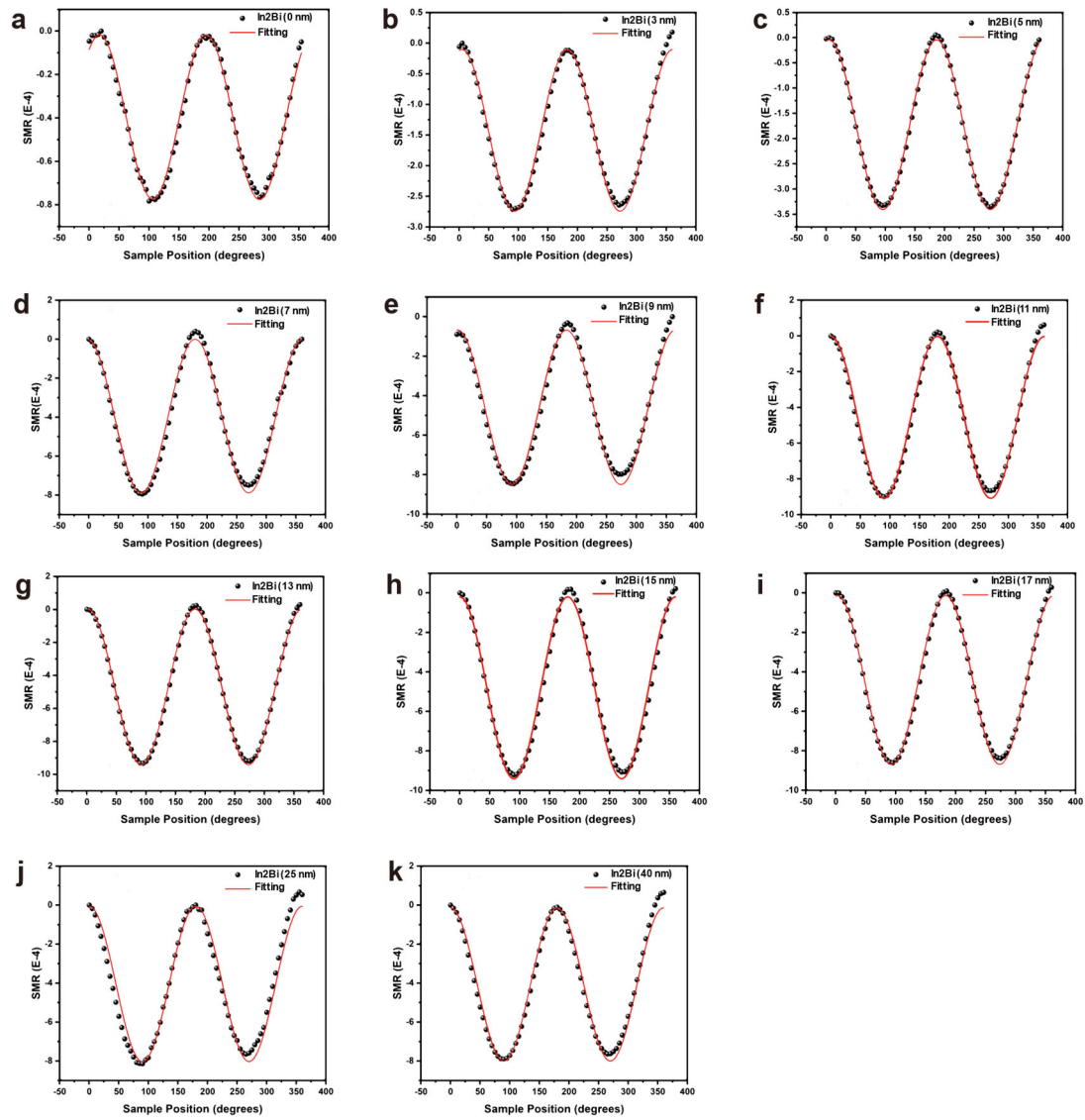


Fig. S5. a-k, SMR curves of Co (3)/In₂Bi (t) in different In₂Bi thickness, $t = 0$ nm, 3 nm, 5 nm, 7 nm, 9 nm, 11 nm, 13 nm, 15 nm, 17 nm, 25 nm and 40 nm.

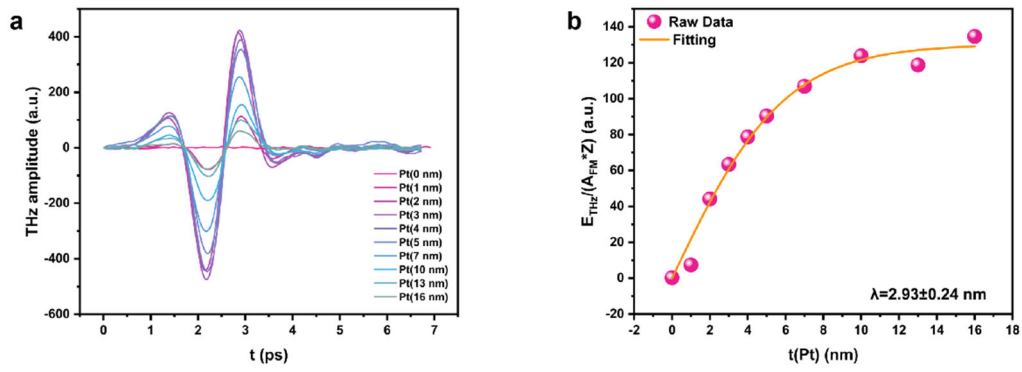


Fig. S6. a, THz emission test of Co (3)/Pt (t)/Al₂O₃ sample. **b**, The Pt thickness dependence of the THz amplitude for Co (3)/Pt (t)/Al₂O₃ spintronic THz emitter. The symbols and lines reveal the experimental and theoretical results, respectively.

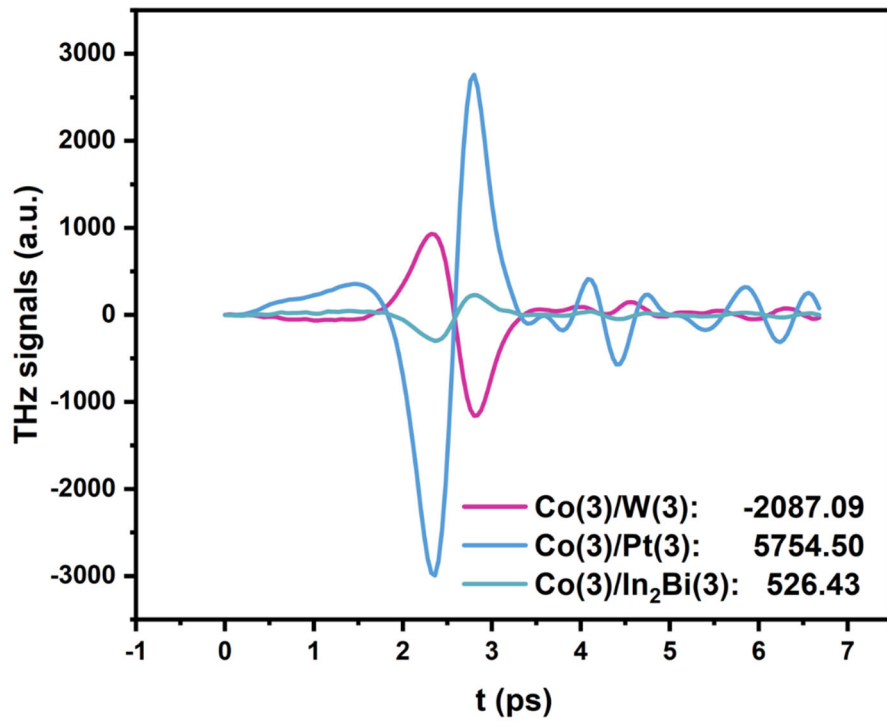


Fig. S7. THz emission signals of Co (3)/W (3), Co (3)/Pt (3) and Co (3)/In₂Bi (3) heterojunctions measured under the same conditions. The results show that the spin current direction of In₂Bi is the same as that of Pt but opposite to that of W.

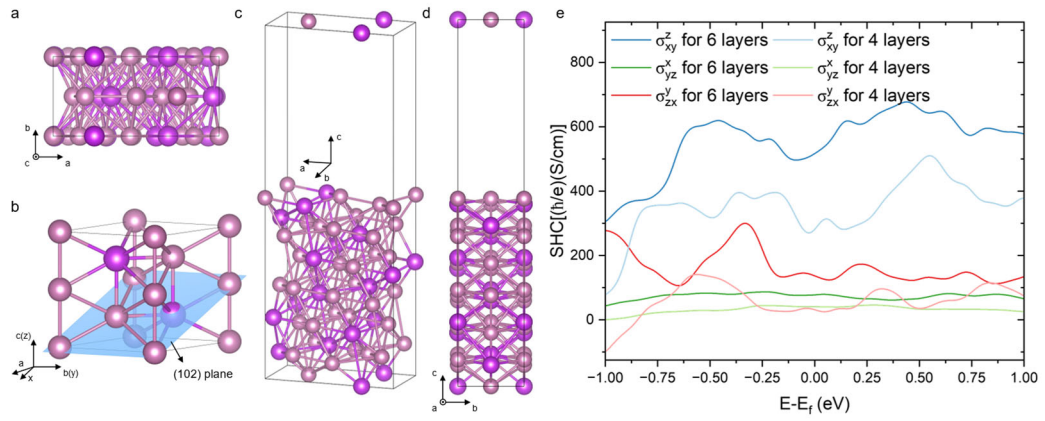


Fig. S8 Crystal structure and SHC of In₂Bi in phase (102). **a-d**, The crystal structure of In₂Bi in phase (102) with 4-atom-layer. **e**, Three main non-zero quantities in the SHC tensor plotted as a function of energy. The high and low saturation color groups represent the results of 6-layer and 4-layer structure, respectively.

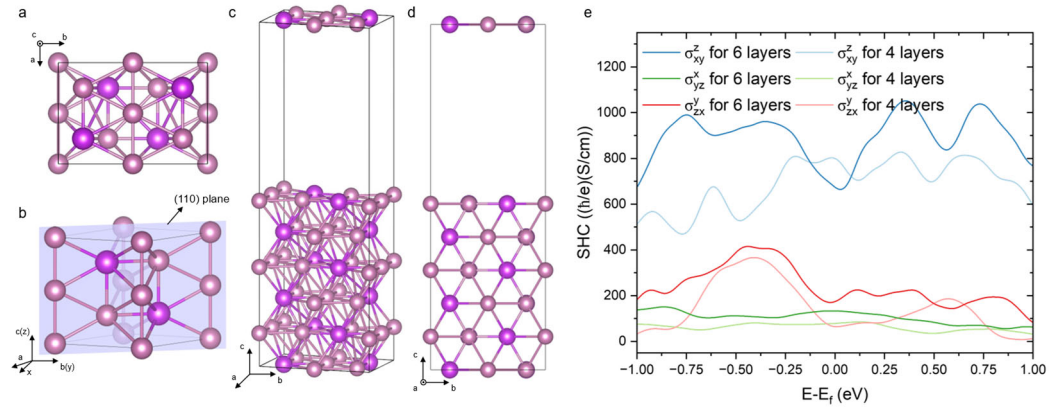


Fig. S9 Crystal structure and SHC of In₂Bi in phase (110). **a-d**, The crystal structure of In₂Bi in phase (110) with 4-atom-layer. **e**, Three main non-zero quantities in the SHC tensor plotted as a function of energy. The high and low saturation color groups represent the results of 6-layer and 4-layer structure, respectively.

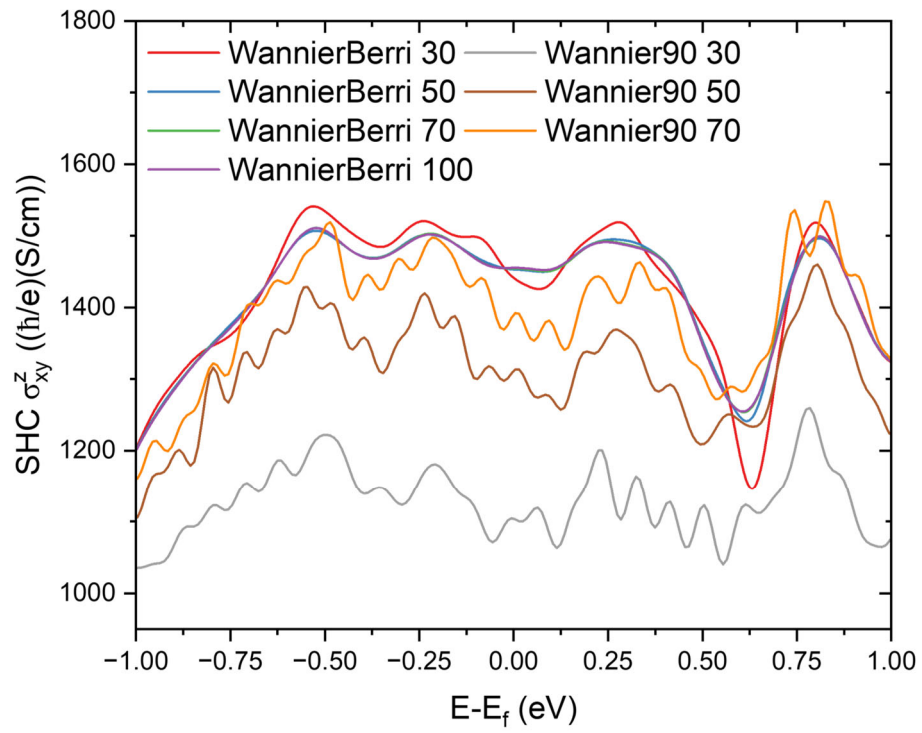


Fig. S10. Comparison of two calculated method and corresponding k-mesh converge test.

The legend indicates the calculation method first, and then the corresponding k-point grid.

Table S1: Different thicknesses in NM layers and corresponding THz signal intensities

| Co (3)/In₂Bi (t) | | Co (3)/Pt (t) | |
|------------------------------------|------------------------------|---------------------------|------------------------------|
| Thickness (nm) | THz Signal (a.u.) | Thickness (nm) | THz Signal (a.u.) |
| 0 | 3.8 | 0 | 10.2 |
| 3 | 84.7 | 1 | 190.9 |
| 5 | 163.8 | 2 | 856.8 |
| 7 | 218.6 | 3 | 898.0 |
| 9 | 260.8 | 4 | 834.5 |
| 11 | 280.0 | 5 | 736.0 |
| 13 | 299.0 | 7 | 557.3 |
| 15 | 287.2 | 10 | 345.1 |
| 17 | 282.0 | 13 | 202.4 |
| 19 | 264.8 | 16 | 138.3 |
| 30 | 237.6 | | |
| 40 | 178.6 | | |

Reference

1. M. C. Beeler et al., The spin Hall effect in a quantum gas. *Nature* **498**, 201-204 (2013).
2. I. A. Ado, A. Qaiumzadeh, R. A. Duine, A. Brataas, M. Titov, Asymmetric and Symmetric Exchange in a Generalized 2D Rashba Ferromagnet. *Phys. Rev. Lett.* **121**, 086802 (2018).
3. Z. G. Yu, Spin-Orbit Coupling, Spin Relaxation, and Spin Diffusion in Organic Solids. *Phys. Rev. Lett.* **106**, 106602 (2011).
4. D. Chiba, M. Yamanouchi, F. Matsukura, H. Ohno, Electrical manipulation of magnetization reversal in a ferromagnetic semiconductor. *Science* **301**, 943-945 (2003).
5. Y. Wang et al., Magnetization switching by magnon-mediated spin torque through an antiferromagnetic insulator. *Science* **366**, 1125-1128 (2019).
6. Y. Fan et al., Magnetization switching through giant spin-orbit torque in a magnetically doped topological insulator heterostructure. *Nat. Mater.* **13**, 699-704 (2014).
7. H. Wang et al., Room temperature energy-efficient spin-orbit torque switching in two-dimensional van der Waals Fe₃GeTe₂ induced by topological insulators. *Nat. Commun.* **14**, 5173 (2023).
8. L. You et al., Switching of perpendicularly polarized nanomagnets with spin orbit torque without an external magnetic field by engineering a tilted anisotropy. *Proceedings of the National Academy of Sciences* **112**, 10310-10315 (2015).
9. C. H. Jin et al., Imaging of pure spin-valley diffusion current in WS₂/WSe₂ heterostructures. *Science* **360**, 893-896 (2018).
10. P. Vaidya et al., Subterahertz spin pumping from an insulating antiferromagnet. *Science* **368**, 160-165 (2020).
11. A. Manchon et al., Current-induced spin-orbit torques in ferromagnetic and antiferromagnetic systems. *Reviews of Modern Physics* **91**, 035004 (2019).
12. M. Dc et al., Room-temperature high spin-orbit torque due to quantum confinement in sputtered BixSe(1-x) films. *Nat. Mater.* **17**, 800-807 (2018).
13. J. X. Li et al., Spin current from sub-terahertz-generated antiferromagnetic magnons. *Nature* **578**, 70-74 (2020).
14. R. Yu et al., Determination of spin Hall angle and spin diffusion length in β -phase-dominated tantalum. *Physical Review Materials* **2**, 074406 (2018).
15. J. Kim, P. Sheng, S. Takahashi, S. Mitani, M. Hayashi, Spin Hall Magnetoresistance in Metallic Bilayers. *Phys. Rev. Lett.* **116**, 097201 (2016).
16. P. Sheng et al., The spin Nernst effect in tungsten. *Science advances* **3**, e1701503 (2017).
17. E.-S. Park et al., Strong higher-order angular dependence of spin-orbit torque in W/CoFeB bilayer. *Physical Review B* **107**, 064411 (2023).
18. Y. Li et al., Enhancing the Spin-Orbit Torque Efficiency by the Insertion of a Sub-nanometer β -W Layer. *ACS Nano* **16**, 11852-11861 (2022).
19. J. W. Lee et al., Enhanced spin-orbit torque by engineering Pt resistivity in Pt/Co/AIO structures. *Physical Review B* **96**, 064405 (2017).
20. M. Fang et al., Tuning the interfacial spin-orbit coupling with ferroelectricity. *Nat. Commun.* **11**, 2627 (2020).
21. M. Isasa, E. Villamor, L. E. Hueso, M. Gradhand, F. Casanova, Temperature dependence

- of spin diffusion length and spin Hall angle in Au and Pt. *Physical Review B* **91**, 024402 (2015).
22. X. K. Xu et al., Giant Extrinsic Spin Hall Effect in Platinum-Titanium Oxide Nanocomposite Films. *Advanced Science* **9**, 9 (2022).
 23. M. V. Berry, Quantal phase factors accompanying adiabatic changes. Proceedings of the Royal Society of London. A. *Mathematical Physical Sciences* **392**, 45-57 (1984).
 24. C. L. Kane, E. J. Mele, Quantum Spin Hall Effect in Graphene. *Phys. Rev. Lett.* **95**, 226801 (2005).
 25. D. J. Thouless, M. Kohmoto, M. P. Nightingale, M. den Nijs, Quantized Hall Conductance in a Two-Dimensional Periodic Potential. *Phys. Rev. Lett.* **49**, 405-408 (1982).
 26. D. Xiao, M.-C. Chang, Q. Niu, Berry phase effects on electronic properties. *Reviews of Modern Physics* **82**, 1959-2007 (2010).
 27. Y. Zhang et al., Different types of spin currents in the comprehensive materials database of nonmagnetic spin Hall effect. *npj Computational Materials* **7**, 167 (2021).
 28. F. Schindler et al., Higher-order topology in bismuth. *Nat. Phys.* **14**, 918-924 (2018).
 29. R. Noguchi et al., Evidence for a higher-order topological insulator in a three-dimensional material built from van der Waals stacking of bismuth-halide chains. *Nat. Mater.* **20**, 473-479 (2021).
 30. Y. Lu et al., Topological Properties Determined by Atomic Buckling in Self-Assembled Ultrathin Bi(110). *Nano Lett.* **15**, 80-87 (2015).
 31. Y. Zhang et al., Spin Nernst effect in a p-band semimetal InBi. *New Journal of Physics* **22**, 093003 (2020).
 32. M.-H. Nguyen, D. C. Ralph, R. A. Buhrman, Spin Torque Study of the Spin Hall Conductivity and Spin Diffusion Length in Platinum Thin Films with Varying Resistivity. *Phys. Rev. Lett.* **116**, 126601 (2016).
 33. Y. Wang, P. Deorani, X. Qiu, J. H. Kwon, H. Yang, Determination of intrinsic spin Hall angle in Pt. *Appl. Phys. Lett.* **105**, 152412 (2014).
 34. P. Wang et al., Inverse orbital Hall effect and orbitronic terahertz emission observed in the materials with weak spin-orbit coupling. *npj Quantum Materials* **8**, 28 (2023).
 35. H. Zhang et al., Laser pulse induced efficient terahertz emission from Co/Al heterostructures. *Physical Review B* **102**, 024435 (2020).
 36. L. Zhu, D. C. Ralph, R. A. Buhrman, Highly Efficient Spin-Current Generation by the Spin Hall Effect in Au(1-x)P(x). *Physical Review Applied* **10**, 031001 (2018).
 37. M. Kawaguchi, D. Towa, Y.-C. Lau, S. Takahashi, M. Hayashi, Anomalous spin Hall magnetoresistance in Pt/Co bilayers. *Appl. Phys. Lett.* **112**, 152412 (2018).
 38. J. Qin, D. Hou, Y. Chen, E. Saitoh, X. Jin, Spin Hall magnetoresistance in Pt/Cr₂O₃/YIG structure. *J. Magn. Magn. Mater.* **534**, 167980 (2021).
 39. J. Qiao, J. Zhou, Z. Yuan, W. Zhao, Calculation of intrinsic spin Hall conductivity by Wannier interpolation. *Physical Review B* **98**, 214402 (2018).
 40. X. Zhang, S. Li, A. Wang, H. Bao, Pressure-dependent thermal conductivity in Al, W, and Pt: Role of electrons and phonons. *Physical Review B* **106**, 094313 (2022).
 41. Y. Wang, P. Deorani, X. Qiu, J. H. Kwon, H. Yang, Determination of intrinsic spin Hall angle in Pt. *Applied Physics Letters* **105**, 152412 (2014).
 42. P. Giannozzi *et al.*, Advanced capabilities for materials modelling with Quantum ESPRESSO.

- Journal of Physics: Condensed Matter* **29**, 465901 (2017).
43. P. Giannozzi *et al.*, QUANTUM ESPRESSO: a modular and open-source software project for quantum simulations of materials. *Journal of Physics: Condensed Matter* **21**, 395502 (2009).
 44. A. Dal Corso, Pseudopotentials periodic table: From H to Pu. *Computational Materials Science* **95**, 337-350 (2014).
 45. N. Marzari, A. A. Mostofi, J. R. Yates, I. Souza, D. Vanderbilt, Maximally localized Wannier functions: Theory and applications. *Reviews of Modern Physics* **84**, 1419-1475 (2012).
 46. J. Qiao, J. Zhou, Z. Yuan, W. Zhao, Calculation of intrinsic spin Hall conductivity by Wannier interpolation. *Physical Review B* **98**, 214402 (2018).
 47. S. S. Tsirkin, High performance Wannier interpolation of Berry curvature and related quantities with WannierBerri code. *npj Computational Materials* **7**, 1-9 (2021).
 48. S. Poncé, E. R. Margine, C. Verdi, F. Giustino, EPW: Electron-phonon coupling, transport and superconducting properties using maximally localized Wannier functions. *Computer Physics Communications* **209**, 116-133 (2016).
 49. D. R. Hamann, Optimized norm-conserving Vanderbilt pseudopotentials. *Physical Review B* **88**, 085117 (2013).
 50. S. Baroni, S. de Gironcoli, A. Dal Corso, P. Giannozzi, Phonons and related crystal properties from density-functional perturbation theory. *Reviews of Modern Physics* **73**, 515-562 (2001).
 51. A. A. Mostofi *et al.*, An updated version of wannier90: A tool for obtaining maximally-localised Wannier functions. *Computer Physics Communications* **185**, 2309-2310 (2014).
 52. T. Seifert *et al.*, Efficient metallic spintronic emitters of ultrabroadband terahertz radiation. *Nat. Photonics* **10**, 483-488 (2016).
 53. J. Walowski, M. Münzenberg, Perspective: Ultrafast magnetism and THz spintronics. *J. Appl. Phys.* **120**, (2016).
 54. M. Battiato, K. Carva, P. M. Oppeneer, Superdiffusive Spin Transport as a Mechanism of Ultrafast Demagnetization. *Phys. Rev. Lett.* **105**, 027203 (2010).
 55. A. Melnikov *et al.*, Ultrafast Transport of Laser-Excited Spin-Polarized Carriers in Au/Fe/MgO (001). *Phys. Rev. Lett.* **107**, 076601 (2011).